



OPEN

SUBJECT AREAS:
CONJUGATED POLYMERS
CHEMISTRYReceived
16 December 2013Accepted
3 March 2014Published
18 March 2014Correspondence and
requests for materials
should be addressed to
L.D.L. (lidong@mater.
ustb.edu.cn)

Hybrid silver nanoparticle/conjugated polyelectrolyte nanocomposites exhibiting controllable metal-enhanced fluorescence

Xiaoyu Wang, Fang He, Xi Zhu, Fu Tang & Lidong Li

State Key Laboratory for Advanced Metals and Materials, School of Materials Science and Engineering, University of Science and Technology Beijing, Beijing 100083, P. R. China.

Metal-enhanced fluorescence of conjugated polyelectrolytes (CPs) is realized using a simple, green hybrid Ag nanocomposite film. Ag nanoparticles (Ag NPs) are pre-prepared by sodium citrate reduction and incorporated into agarose by mixing to form an Ag-containing agarose film (Ag@agarose). Through variation of the amount of Ag NPs in the Ag@agarose film as well as the thickness of the interlayer between CPs and the Ag@agarose film prepared of layer-by-layer assembly of chitosan and sodium alginate, a maximum 8.5-fold increase in the fluorescence of CPs is obtained. After introducing tyrosinase, this system also can be used to detect phenolic compounds with high sensitivity and good visualization under ultraviolet light.

Fluorescence detection has been widely applied in chemical and biological sensors because of its high sensitivity and effectiveness^{1,2}. During fluorescence detection, the intensity of fluorescence from a fluorophore plays a crucial role. As a result, much effort has been devoted to increasing fluorescence intensity by preparing novel fluorescent materials with high quantum yield, such as organic small-molecule dyes^{3,4}, quantum dots (QDs)^{5,6}, and conjugated polymers^{7,8}. However, most of the reported materials require complicated synthetic procedures. Recently, a different strategy, metal-enhanced fluorescence (MEF), was employed to enhance the fluorescence intensity of fluorophores. MEF is induced by the interactions between fluorophores and surface plasmon resonance (SPR) from adjacent metallic nanostructures^{9–11}. MEF can be controlled by designing a suitable metallic nanostructure, an appropriate interaction region and the optical properties of various fluorophores including organic fluorophores¹², inorganic QDs¹³, and fluorescent proteins¹⁴. Previous studies have demonstrated that the SPR of metallic nanostructures can be changed by altering nanoparticle size, size distribution, shape, composition and surrounding dielectric^{15–18}. To date, a variety of metal species including silver (Ag), gold, aluminum, copper, and zinc have been used to fabricate nanostructures for application in MEF^{19–23}. Among them, nanostructured Ag is a commonly used material because its SPR is typically in the visible region with a high scattering efficiency, and strong MEF activity^{11,24}. Nanostructured Ag films that induce MEF have been fabricated by numerous approaches such as thermal evaporation²⁵, photodeposition²⁶, adsorption of metal colloid²⁷, galvanic cell reactions²⁸ and *in situ* reduction of silver nitrate²⁹. However, these approaches normally involve complicated synthetic procedures. They also use toxic chemicals and allow little control of the scale and surface morphologies of Ag films, which limits their application in MEF systems. Therefore, methods to fabricate nanostructured Ag films with improved control are needed to meet the demands of MEF applications.

Recently, conjugated polyelectrolytes (CPs) have emerged as an attractive fluorophore for chemo/biosensors. CPs possess π -conjugated backbones, large absorption cross sections, good photostability and higher fluorescence relative to small molecules^{30–32}. The charged side chains of CPs endow them with sufficient water solubility³³. The advantages of CPs mean that they can be used in solid detection platforms to detect multiple targets in a single experiment^{34,35}. Layer-by-layer (LbL) assembly, which provides binding sites for ionic dyes or biological agents, can be used to incorporate charged CPs onto the surface of Ag films. By exploiting the MEF effect of nanostructured Ag films, the fluorescence intensity and photostability of CPs could be improved and the sensitivity of CP-based fluorescence detection could be enhanced. Moreover, the MEF effect on nanostructured Ag film

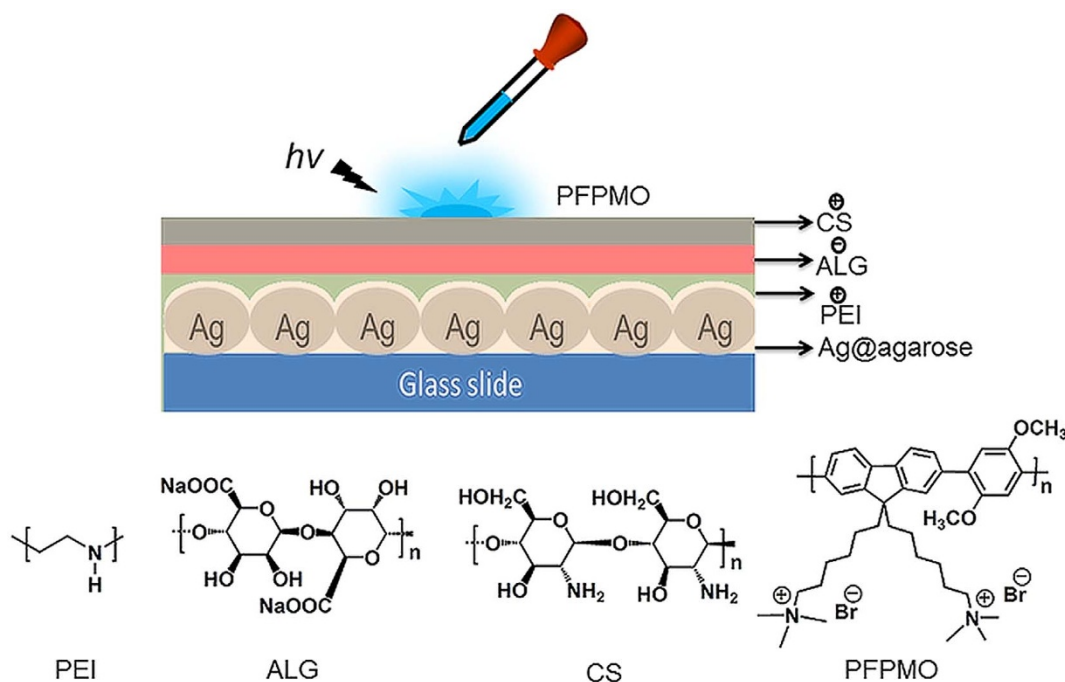


Figure 1 | Structure of the system platform. Chemical structures of polyethylenimine (PEI), chitosan (CS), sodium alginate (ALG) and poly[9,9'-bis(6''-(N,N,N-trimethylammonium)-hexyl)fluorene-co-alt-2,5-dimethoxy-1,4-phenylene dibromide] (PFPMO).

surfaces is strongly distance dependent^{36–38}. LbL assembly, which enables exact deposition of nanometer-thick layers on planar surfaces, can be used to fine-tune the distance between CPs and metal nanostructures^{39–41}.

In this research, we design a facile, green method to fabricate hybrid Ag nanocomposite films to enhance the fluorescence of CPs based on MEF. The SPR of the metallic nanostructures is tuned by simply changing the amount of Ag nanoparticles (NPs) in the film. Moreover, by using biocompatible chitosan (CS)/sodium alginate (ALG) multilayers, it is easy to adjust the interaction distance of the MEF effect by varying thickness. By introducing tyrosinase into the nanocomposite, this system can be used to detect phenolic compounds with high sensitivity and ready visualization under ultraviolet (UV) light.

Results

Preparation and characterization of Ag-containing agarose films.

Figure 1 shows the structure of the system. First, the prepared Ag NPs were loaded onto the agarose matrix structure to form an Ag-containing agarose film (Ag@agarose), which acted as a metallic substrate. Then, a thin layer of cationic polyethylenimine (PEI) was deposited to improve the ability of the structure to form an assembly. Anionic polyelectrolyte ALG and cationic polyelectrolyte CS were deposited stepwise by LbL assembly to form an interlayer. Finally, the fluorescent cationic CP poly[9,9'-bis(6''-(N,N,N-trimethylammonium)-hexyl)fluorene-co-alt-2,5-dimethoxy-1,4-phenylene dibromide]⁴² (PFPMO) was added dropwise onto the interlayer surface in a controlled manner. The Ag/PFPMO nanocomposite film possessed a positively charged surface. The corresponding photographs of quartz slide, Ag@agarose and Ag/PFPMO films showed the assemble process (see Supplementary Fig. S1 online).

Ag NPs were synthesized in one step according to a reported procedure⁴³. The concentration of Ag NPs was around 3×10^7 NPs/ μL ⁴⁴. The advantages of this method are that Ag NPs reduced and stabilized with non-toxic sodium citrate are more environmentally friendly and reactive than those formed by the seeded growth method using a toxic reducing agent. In addition, the large Ag

NPs prepared by this method displayed obvious SPR^{45,46}. A TEM image of the Ag NPs is depicted in Fig. 2a. The synthesized Ag NPs are monodisperse, with an average diameter of 65 nm, which is suitable to generate a MEF effect⁴⁵. In addition, the Ag NPs exhibit a ζ -potential of -37.5 mV, which is high enough to enable stabilization of the NPs in aqueous solution. To consider the fundamental relationship between SPR and light absorption, the UV-Vis absorption spectrum of the Ag NPs in aqueous solution was measured, as shown in Fig. 2b. The NPs exhibit a characteristic absorption peak at approximately at 410 nm, which is consistent with the SPR band of spherical Ag NPs in aqueous solution⁴⁷.

Agarose can form a physically crosslinked gel network involving hydrogen bonding and hydrophobic interactions upon cooling its hot aqueous solution to room temperature⁴⁸. Because of its good film-forming ability and biocompatibility, agarose was selected to immobilize Ag NPs on the platform. By directly mixing different amounts of the Ag NP solution with 0.5% agarose solution, seven types of Ag@agarose film with different concentrations of Ag NPs in the range of $0.15\text{--}3 \times 10^6$ NPs/ μL were prepared. The content of Ag NPs in the agarose films was monitored by UV-Vis absorption spectroscopy. As shown in Fig. 3a, no obvious absorbance peak was observed from the bare agarose film. At a low Ag NP concentration of 0.15×10^6 NPs/ μL , a distinct absorbance peak emerged at

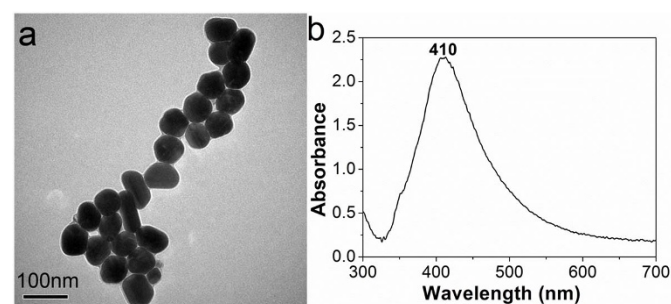


Figure 2 | Properties of prepared Ag NPs. (a) TEM image and (b) UV-Vis absorption spectrum of Ag NPs in solution.

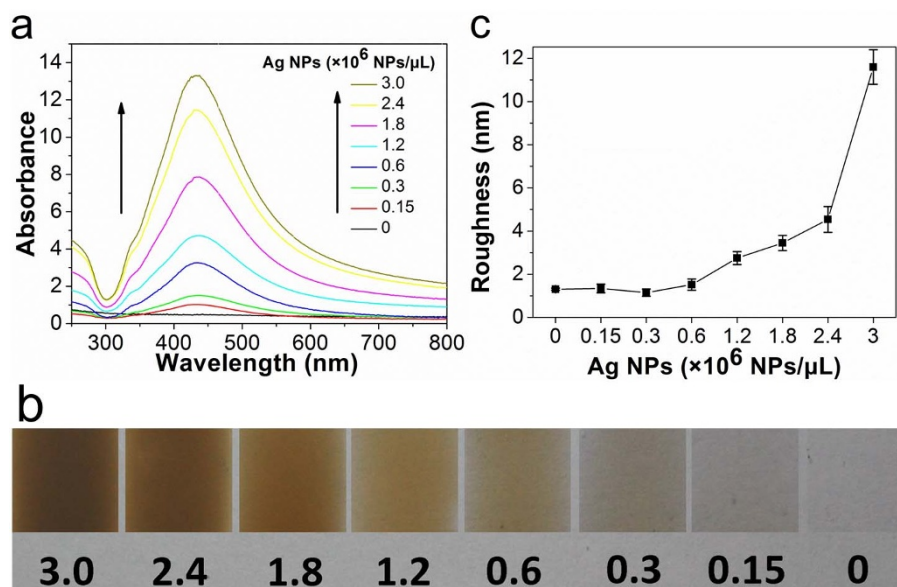


Figure 3 | Characterization of Ag-containing agarose films. (a) UV-visible absorption spectra, (b) photographs, and (c) roughness of the Ag@agarose films with different Ag NP concentrations ranging from 0–3 $\times 10^6$ NPs/ μL . Error bars correspond to the standard deviation determined from ten separate measurements.

433 nm, which is attributed to the SPR band of Ag NPs in the Ag@agarose film. The absorption intensity of Ag NPs increase gradually with Ag NP concentration and the absorption maxima remained at 433 nm. The result reveals that agarose can act as an effective support material to immobilize Ag NPs on the platform. Meanwhile, because of their protection with citrate, the Ag NPs were stabilized in agarose, which allowed highly concentrated NP dispersions to form. However, the absorption maximum of the Ag NPs shifted from 410 nm in aqueous solution to 433 nm in the Ag@agarose film. It is known that the SPR of metal NPs depends on the dielectric properties of the surrounding medium^{49,50}. Therefore, this red shift was mainly related to the different dielectric environments of the aqueous solution and agarose film. The color of the Ag@agarose films (Fig. 3b) gradually changed from transparent to deep brown as the concentration of Ag NPs increased, which further indicates that Ag NPs were densely packed on the substrate.

The surface morphologies of Ag@agarose films were analyzed by AFM (see Supplementary Fig. S2 online). As the concentration of Ag NPs increased up to 1.8×10^6 NPs/ μL , Ag NPs gradually spread over the surface and formed a homogeneous structure. The corresponding roughness of the films increased slightly from 1 to 3.45 nm (Fig. 3c). However, as the concentration of Ag NPs increased further to 3×10^6 NPs/ μL , the homogeneous structure was disrupted and uniformity decreased. The corresponding roughness of the films increased dramatically to 11.6 nm. High coverage and a uniform surface will result in an efficient MEF effect^{28,51}, so the Ag@agarose film with 1.8×10^6 NPs/ μL was selected as the metallic substrate in our study because of its dense, homogeneous Ag structure.

MEF effect of an Ag/PFPMO nanocomposite film. The fluorescence intensity of a fluorophore depends not only on the amount of Ag NPs on the substrate, but also on the distance between CPs and metal nanostructures. Therefore, it is important to optimize the distance for efficient MEF. PFPMO was chosen as a fluorophore because its emission spectrum overlaps well with the absorption spectrum of the Ag@agarose film, which should allow efficient MEF (Fig. 4a)^{52,53}. In addition, PFPMO possesses good water solubility and multiple charges, so it is easy to assemble on the polyelectrolyte surface.

Ag@agarose films containing 1.8×10^6 NPs/ μL with uniform surface were used to determine the fluorescence intensity of PFPMO at different distances from the Ag@agarose film surface. Four different PEI/(ALG/CS)_n ($n = 0-3$) interlayers were prepared by LbL assembly using electrostatic attraction. The obtained interlayers are denoted PEI, PEI-1BL, PEI-2BL and PEI-3BL. Fig. 4b illustrates the fluorescence intensity of PFPMO at different distances from the surface of agarose and Ag@agarose films. Without Ag NPs, the fluorescence intensity of PFPMO at different distances from the agarose film surface remained similar. Conversely, in the presence of Ag NPs, the fluorescence intensity of PFPMO changed markedly with distance. When PFPMO was directly attached onto the surface of the Ag@agarose film, the fluorescence intensity was quenched. One PEI interlayer caused the fluorescence intensity of PFPMO to increase slightly. When the interlayer was changed to one bilayer, the fluorescence intensity of PFPMO reached its maximum. Further increasing the thickness of the interlayer caused the fluorescence intensity of PFPMO to decrease. These results show that MEF depends strongly on the distance between PFPMO and the Ag@agarose film. The thicknesses of the initial PEI layer and each CS/ALG bilayer were 1.3 and 9.2 nm, respectively. Because the PEI-1BL interlayer exhibited the largest MEF effect, the optimal interaction distance in our MEF system is around 10.5 nm. The presence of a PEI-1BL interlayer on the Ag@agarose film with 1.8×10^6 NPs/ μL smoothed the surface of the film (see Supplementary Fig. S3 online), indicating that this interlayer was successfully assembled by electrostatic attraction.

We also studied the fluorescence spectra of PFPMO on different substrates (Fig. 4c). A large enhancement of ~ 8.5 -fold was observed for PFPMO on Ag@agarose/PEI-1BL film compared with that on a glass/PEI-1BL film, while the fluorescence intensity of PFPMO was quenched by about 17% on an agarose/PEI-1BL film compared with that on the glass/PEI-1BL film. When PFPMO was deposited directly on glass, the fluorescence of PFPMO was quenched by about 40% due to the self-aggregation compared with that on the glass/PEI-1BL film. These results indicate that the Ag@agarose film was suitable as a metallic substrate to realize MEF and PFPMO had desirable fluorescent properties on this substrate. The noticeable enhancement of the intensity of fluorescence from PFPMO on the Ag@agarose substrate could be visually observed by the naked

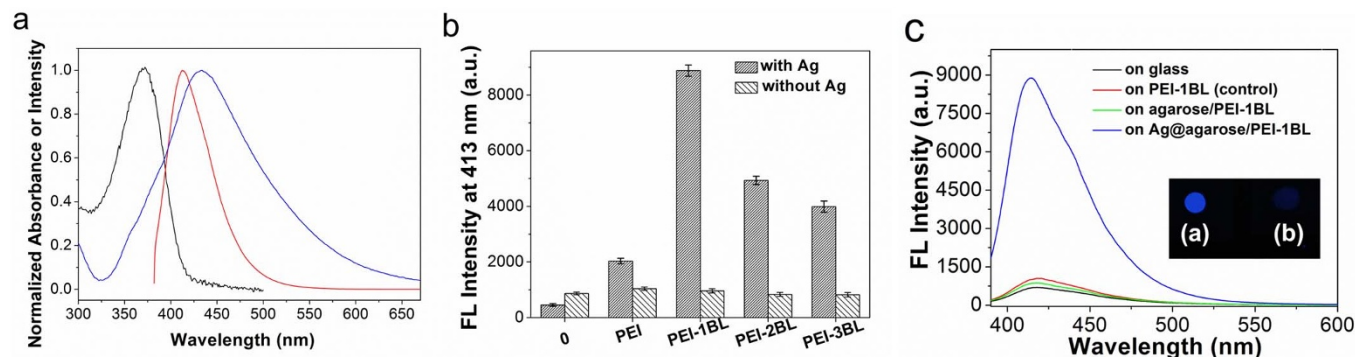


Figure 4 | MEF effect in Ag/PFPMO nanocomposite films. (a) Normalized absorption (black) and fluorescence spectra (red) of PFPMO in water upon excitation at 362 nm, and normalized absorption spectrum (blue) of Ag NPs in agarose. (b) The effect of interlayer thickness on the emission intensity of PFPMO in the presence and absence of an Ag@agarose film with 1.8×10^6 NPs/ μL . PEI-1BL, PEI-2BL and PEI-3BL are PEI/(ALG/CS), PEI/(ALG/CS)₂ and PEI/(ALG/CS)₃ interlayer films, respectively. (c) Emission spectra of PFPMO on different substrates. Inset: fluorescence photographs of (a) on Ag@agarose/PEI-1BL and (b) on PEI-1BL following irradiation at 365 nm. The excitation wavelength was 362 nm. Error bars correspond to the standard deviation calculated from three separate measurements.

eye under UV light (inset in Fig. 4c). Therefore, the Ag/PFPMO nanocomposite film with a PEI-1bilayer interlayer assembled on the Ag@agarose film with 1.8×10^6 NPs/ μL was optimal for our MEF system.

Detection of phenolic compounds by Ag/PFPMO nanocomposite films. We then examined the ability of this MEF system to detect phenolic compounds. Tyrosinase was adsorbed onto the surface of the film by electrostatic attraction because CS and PFPMO provide a positively charged surface. Tyrosinase can be used to catalyze the oxidation of phenolic compounds to quinone (see Supplementary Fig. S4 online), which is capable of quenching the emission of CPs *via* electron transfer⁵⁴. As a result, phenolic compounds can be detected by monitoring the quenching of PFPMO by the produced quinone. Six kinds of phenolic compounds were chosen for detection: bisphenol A (BPA), catechol, dopamine, phenol, p-cresol and m-cresol. Fig. 5a illustrates the change of I/I_0 with reaction time in the presence of 10 μM of different phenolic compounds, where I and I_0 represent the fluorescence intensity of PFPMO at 413 nm in the presence and absence of phenolic compounds, respectively. After addition of different phenolic compounds, the fluorescence emission

intensity of PFPMO decreased with reaction time because of the formation of quinones. The degree of fluorescence quenching reached its maximum value after ~ 20 min for catechol and dopamine, and ~ 30 min for BPA, phenol, p-cresol and m-cresol. Among these compounds, the quenching efficiency of BPA is 85%, which is slightly higher than those of the other phenols. Comparing the structures of these phenolic compounds reveals that the faster reaction for catechol and dopamine is caused by a one-step enzymatic process involving direct conversion of catechol to quinone, while for the other compounds, the reaction is slower because the enzymatic process involves multiple steps: the conversion of phenolic substrates to catechol, followed by quinone formation. Unlike the other phenols investigated here, BPA contains two phenolic rings per molecule. Therefore, BPA formed two quinone-like structures at the two rings, whereas the others produced one, which resulted in stronger quenching of BPA. However, the fluorescence intensity of PFPMO was quenched by more than 75% for all of these compounds, demonstrating that fluorescence quenching by quinone is a general phenomenon. The developed system is suitable to detect all of these well-known phenolic compounds.

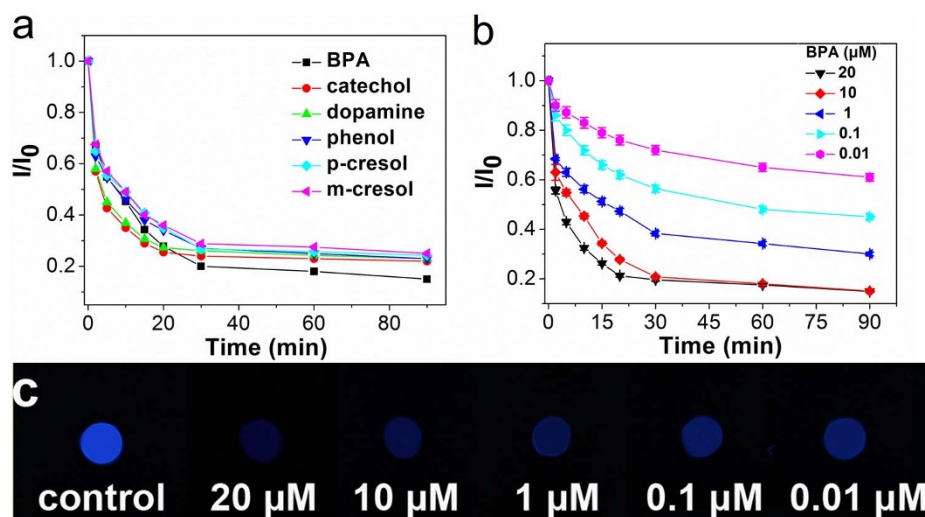


Figure 5 | Detection of phenolic compounds on Ag/PFPMO nanocomposite films. (a) Change of I/I_0 as a function of time in the presence of 10 μM of different phenolic compounds. (b) Change of I/I_0 as a function of time in the presence of different concentrations of BPA. (c) Fluorescence photographs of PFPMO under 365-nm UV light in the presence of different concentrations of BPA. Error bars correspond to the standard deviation calculated from three separate measurements.



Then, we chose BPA as a model to evaluate the sensitivity of this detection protocol. The change of I/I_0 with reaction time in the presence of different concentrations of BPA is shown in Fig. 5b. For the entire range of BPA concentration examined, the fluorescence intensity of PFPMO decreased with reaction time. Moreover, the emission intensity of PFPMO decreased almost linearly up to a certain concentration of BPA ($\sim 10 \mu\text{M}$), and reached a plateau at higher BPA concentration. Fig. 5c shows that a noticeable intensity change in the system could be detected by the naked eye under UV light, unlike that of the blank. This system allows sensitive detection of BPA with a low detection limit of $0.01 \mu\text{M}$.

Discussion

In this work, a simple, green Ag nanocomposite film was prepared to enhance the fluorescence intensity of the CP PFPMO. Non-toxic sodium citrate functions as a reductant and stabilizing agent to synthesize large Ag NPs that exhibit a large scattering cross-section, which benefits the MEF effect. Polysaccharide agarose serves as a support material because of its good film-forming ability and low background fluorescence. By direct mixing, Ag NPs were well dispersed and densely loaded onto polysaccharide agarose to form Ag@agarose films. The surface morphologies of Ag@agarose films can be controlled by the content of Ag NPs. The optimized Ag concentration in the Ag@agarose films is 1.8×10^6 NPs/ μL and the formed homogeneous Ag structure helps to enhance PFPMO fluorescence. The resulting Ag@agarose film exhibited tunable fluorescence enhancement of PFPMO that could be controlled simply by varying the distance between PFPMO and Ag@agarose. Conventional LbL assembly of natural polysaccharide CS and ALG was successfully utilized to produce the desired MEF effect, achieving a maximum 8.5-fold increase in the fluorescence intensity of PFPMO with an interlayer of PEI-1BL.

The resulting Ag/PFPMO nanocomposite film provides a biocompatible environment for tyrosinase as well as an extensively charged surface to immobilize it. The enhanced fluorescence intensity of PFPMO was used to detect phenolic compounds. After addition of phenolic compounds, PFPMO fluorescence intensity was quenched by quinone intermediates produced from the tyrosinase-catalyzed oxidation of the phenolic compounds. The intensity change is concentration dependent and visible to the naked eye under UV light. For BPA, which can disrupt the human endocrine system⁵⁵, the detection limit is as low as $0.01 \mu\text{M}$. Therefore, the system based on an Ag/PFPMO nanocomposite film exhibits enhanced fluorescence intensity and good sensitivity, and is an efficient approach to fluorescence detection. In the current system, phenolic compounds are detected only by quinone-induced fluorescence quenching of CPs. However, using the present method, the fluorescence intensity of CPs was partly quenched. So the analytical sensitivity will be influenced by the remaining fluorescence of CPs. To further obtain much higher analytical sensitivity of the system, our future work will focus on optimization of nanocomposite film structures and modification property of conjugated polymers. It is anticipated that this research can provide a new avenue for enhanced fluorescence detection.

Methods

Materials. PFPMO was synthesized according to a published procedure⁴². Ultrapure agarose, CS, ALG, PEI ($M_r = 55,000$), tyrosinase (from mushroom, 4276 units/mg), and dopamine were purchased from Sigma-Aldrich. Sodium citrate, silver nitrate, phenol, m-cresol, p-cresol, catechol and BPA were purchased from Beijing Chemical Reagent Co. Ltd.

Preparation of Ag@agarose films. Silver nitrate (9.5 mg) was mixed with deionized water (100 mL) at 45°C and heated rapidly until boiling with vigorous stirring. Aqueous sodium citrate (1%, 3 mL) was added, and then the mixture was boiled gently for 90 min while stirring. Ag NPs were collected *via* centrifugation ($5,900 \times g$, 15 min) and dispersed in H_2O (10 mL) with a concentration of 3×10^7 NPs/ μL . Quartz slides (10×10 mm) were immersed in piranha solution ($\text{H}_2\text{O}_2:\text{H}_2\text{SO}_4 = 1:3$

v/v) at 80°C for 30 min, washed three times with deionized water, and then dried under a gentle stream of nitrogen gas. Agarose was dissolved in deionized water (1 mL) at 95°C with stirring to form a 0.5% solution. Then, 0, 5, 10, 20, 40, 60, 80, or 100 μL of the prepared Ag NP solution was added. Aliquots of the hot mixed solution (100 μL) were spread on one side of each quartz slide and dried in air for 4 h.

Preparation of Ag/PFPMO nanocomposite films. The Ag@agarose films were immersed in PEI solution (3 mL, 1 mg/mL) for 10 min to form the first PEI layer, and then alternatively immersed in charged ALG solution (3 mL, 1 mg/mL in deionized water) and CS solution (3 mL, 1 mg/mL in 0.1 M acetic acid) under the same conditions. The final layer was CS. In the experiments, 1–3 bilayers were added to control the thickness of the interlayer films. PFPMO solution (0.1 mM, 1 μL) was added dropwise onto each quartz slide. As a control, an agarose film without Ag NPs was covered with the same interlayers. The spotted slides were dried in air for 60 min at room temperature. MEF was measured by comparing the fluorescence intensities of different samples.

Detection of phenolic compounds on Ag/PFPMO nanocomposite films.

Tyrosinase (2.5 μL , 200 units/ μL) in phosphate buffered saline (25 mM, $\text{pH} = 6.8$) was added dropwise onto each quartz slide. The spotted slides were dried in air for 30 min at room temperature. Different phenolic compounds (10 μL) were incubated on each slide at room temperature for 0–90 min. After drying in air for 60 min at room temperature, images of the microarray were obtained under 365-nm UV light.

Characterization. TEM images of the Ag NPs were observed by a JEM 2100 transmission electron microscope with an accelerating voltage of 120 kV. The concentration of Ag NPs was determined using a combination of TEM images and Agilent 7500 CE inductively coupled plasma mass spectrometry (ICP-MS). The sample was prepared by dissolving the suspension of Ag NPs with concentrated HNO_3 in a level of 100 ppb for ICP-MS analysis. The calculation of Ag NPs concentration is based on the concentration of silver atoms according to the following correlation: Ag NPs concentration = Ag atomic concentration $\times (0.144^3/0.74/R^3)$, where 0.144 is the atomic radius of Ag in nanometer, 0.74 is the packing factor for FCC lattice structure and R is the effective radius of Ag NPs in nanometer. AFM images of the films were recorded by a NanoScope III AFM. UV-Vis absorption spectra were obtained using a Hitachi U3900 spectrophotometer. Fluorescence measurements were obtained at room temperature using a Hitachi F-7000 fluorescence spectrometer with a Xenon lamp excitation. The slit width and photomultiplier tube (PMT) voltages used were 5 nm and 700 V, respectively. Front face emission collection was employed for all films. The thickness of each multilayer film was determined with a surface profilometer (XP-2, Ambios Technology, Santa Cruz, CA) at room temperature. Photographs were taken under 365-nm UV light.

- Davidson, R. S. Application of fluorescence microscopy to a study of chemical problems. *Chem. Soc. Rev.* **25**, 241–253 (1996).
- Thomas III, S. W., Joly, G. D. & Swager, T. M. Chemical sensors based on amplifying fluorescent conjugated polymers. *Chem. Rev.* **107**, 1339–1386 (2007).
- Nolan, E. M. & Lippard, S. J. Small-molecule fluorescent sensors for investigating zinc metalloneurochemistry. *Acc. Chem. Res.* **42**, 193–203 (2009).
- Wang, J., Xu, X., Shi, L. & Li, L. Fluorescent organic nanoparticles based on branched small molecule: preparation and ion detection in lithium-ion battery. *ACS Appl. Mater. Interfaces* **5**, 3392–3400 (2013).
- Bruchez Jr, M., Moronne, M., Gin, P., Weiss, S. & Alivisatos, A. P. Semiconductor nanocrystals as fluorescent biological labels. *Science* **281**, 2013–2016 (1998).
- Larson, D. R. *et al.* Water-soluble quantum dots for multiphoton fluorescence imaging in vivo. *Science* **300**, 1434–1436 (2003).
- Duan, X., Liu, L., Feng, F. & Wang, S. Cationic conjugated polymers for optical detection of DNA methylation, lesions, and single nucleotide polymorphisms. *Acc. Chem. Res.* **43**, 260–270 (2010).
- Jiang, H., Taranehar, P., Reynolds, J. R. & Schanze, K. S. Conjugated polyelectrolytes: synthesis, photophysics, and applications. *Angew. Chem. Int. Ed.* **48**, 4300–4316 (2009).
- Cui, Q., He, F., Li, L. & Mohwald, H. Controllable metal-enhanced fluorescence in organized films and colloidal system. *Adv. Colloid Interface Sci.* (2013). <http://dx.doi.org/10.1016/j.cis.2013.10.011>.
- Kulakovich, O. *et al.* Enhanced luminescence of CdSe quantum dots on gold colloids. *Nano Lett.* **2**, 1449–1452 (2002).
- Sabanayagam, C. R. & Lakowicz, J. R. Increasing the sensitivity of DNA microarrays by metal-enhanced fluorescence using surface-bound silver nanoparticles. *Nucleic Acids Res.* **35**, e13 (2007).
- Tang, F., He, F., Cheng, H. & Li, L. Self-Assembly of conjugated polymer-Ag@SiO₂ hybrid fluorescent nanoparticles for application to cellular imaging. *Langmuir* **26**, 11774–11778 (2010).
- Chan, Y.-H. *et al.* Using patterned arrays of metal nanoparticles to probe plasmon enhanced luminescence of CdSe quantum dots. *ACS Nano* **3**, 1735–1744 (2009).
- Ray, K., Chowdhury, M. H., Szmecinski, H. & Lakowicz, J. R. Metal-enhanced intrinsic fluorescence of proteins on silver nanostructured surfaces toward label-free detection. *J. Phys. Chem. C* **112**, 17957–17963 (2008).
- Sherry, L. J. *et al.* Localized surface plasmon resonance spectroscopy of single silver nanocubes. *Nano Lett.* **5**, 2034–2038 (2005).



16. Link, S. & El-Sayed, M. A. Spectral properties and relaxation dynamics of surface plasmon electronic oscillations in gold and silver nanodots and nanorods. *J. Phys. Chem. B* **103**, 8410–8426 (1999).
17. Murphy, C. J. & Jana, N. R. Controlling the aspect ratio of inorganic nanorods and nanowires. *Adv. Mater.* **14**, 80–82 (2002).
18. Link, S., Mohamed, M. B. & El-Sayed, M. A. Simulation of the optical absorption spectra of gold nanorods as a function of their aspect ratio and the effect of the medium dielectric constant. *J. Phys. Chem. B* **103**, 3073–3077 (1999).
19. Neal, T. D., Okamoto, K. & Scherer, A. Surface plasmon enhanced emission from dye doped polymer layers. *Opt. Express* **13**, 5522–5527 (2005).
20. Eustis, S. & El-Sayed, M. A. Why gold nanoparticles are more precious than pretty gold: Noble metal surface plasmon resonance and its enhancement of the radiative and nonradiative properties of nanocrystals of different shapes. *Chem. Soc. Rev.* **35**, 209–217 (2006).
21. Chowdhury, M. H., Ray, K., Gray, S. K., Pond, J. & Lakowicz, J. R. Aluminum nanoparticles as substrates for metal-enhanced fluorescence in the ultraviolet for the label-free detection of biomolecules. *Anal. Chem.* **81**, 1397–1403 (2009).
22. Zhang, Y., Aslan, K., Previte, M. J. R. & Geddes, C. D. Metal-enhanced fluorescence from copper substrates. *Appl. Phys. Lett.* **90**, 173116 (2007).
23. Aslan, K., Previte, M. J. R., Zhang, Y. & Geddes, C. D. Metal-enhanced fluorescence from nanoparticulate zinc films. *J. Phys. Chem. C* **112**, 18368–18375 (2008).
24. Guo, S.-H. *et al.* The effect of an active substrate on nanoparticle-enhanced fluorescence. *Adv. Mater.* **20**, 1424–1428 (2008).
25. Aroca, R., Kovacs, G. J., Jennings, C. A., Loutfy, R. O. & Vincett, P. S. Fluorescence enhancement from Langmuir-Blodgett monolayers on silver island films. *Langmuir* **4**, 518–521 (1988).
26. Geddes, C. D., Parfenov, A. & Lakowicz, J. R. Photodeposition of silver can result in metal-enhanced fluorescence. *Appl. Spectrosc.* **57**, 526–531 (2003).
27. Aslan, K., Lakowicz, J. R. & Geddes, C. D. Rapid deposition of triangular silver nanoplates on planar surfaces: application to metal-enhanced fluorescence. *J. Phys. Chem. B* **109**, 6247–6251 (2005).
28. Ma, N., Tang, F., Wang, X., He, F. & Li, L. Tunable metal-enhanced fluorescence by stimuli-responsive polyelectrolyte interlayer films. *Macromol. Rapid Comm.* **32**, 587–592 (2011).
29. Tong, L. *et al.* pH- and Thermo-responsive Ag/polyelectrolyte hybrid thin films for tunable metal-enhanced fluorescence. *J. Mater. Chem.* **22**, 8988–8993 (2012).
30. Wang, S. & Bazan, G. C. Optically amplified RNA-protein detection methods using light-harvesting conjugated polymers. *Adv. Mater.* **15**, 1425–1428 (2003).
31. Pecher, J. & Mecking, S. Nanoparticles of conjugated polymers. *Chem. Rev.* **110**, 6260–6279 (2010).
32. Ho, H. A., Najari, A. & Leclerc, M. Optical detection of DNA and proteins with cationic polythiophenes. *Acc. Chem. Res.* **41**, 168–178 (2008).
33. Zhu, C., Liu, L., Yang, Q., Lv, F. & Wang, S. Water-soluble conjugated polymers for imaging, diagnosis, and therapy. *Chem. Rev.* **112**, 4687–4735 (2012).
34. Lv, F., Liu, L. & Wang, S. Signal amplifying optical DNA detection on solid support with fluorescent conjugated polymers. *Curr. Org. Chem.* **15**, 548–556 (2011).
35. Raymond, F. R. *et al.* Detection of target DNA using fluorescent cationic polymer and peptide nucleic acid probes on solid support. *BMC Biotechnol.* **5**, 10 (2005).
36. Campion, A., Gallo, A. R., Harris, C. B., Robota, H. J. & Whitmore, P. M. Electronic energy transfer to metal surfaces: a test of classical image dipole theory at short distances. *Chem. Phys. Lett.* **73**, 447–450 (1980).
37. Kümmerlen, J., Leitner, A., Brunner, H., Aussenegg, F. R. & Wokaun, A. Enhanced dye fluorescence over silver island films: analysis of the distance dependence. *Mol. Phys.* **80**, 1031–1046 (1993).
38. Caruso, F., Lichtenfeld, H., Donath, E. & Möhwald, H. Investigation of electrostatic interactions in polyelectrolyte multilayer films: binding of anionic fluorescent probes to layers assembled onto colloids. *Macromolecules* **32**, 2317–2328 (1999).
39. Nooney, R. I., Stranik, O., McDonagh, C. & MacCraith, B. D. Optimization of plasmonic enhancement of fluorescence on plastic substrates. *Langmuir* **24**, 11261–11267 (2008).
40. Kulakovich, O. *et al.* Improved method for fluorophore deposition atop a polyelectrolyte spacer for quantitative study of distance-dependent plasmon-assisted luminescence. *Nanotechnology* **17**, 5201–5206 (2006).
41. dos Santos, D. S. & Aroca, R. F. Selective surface-enhanced fluorescence and dye aggregation with layer-by-layer film substrates. *Analyst* **132**, 450–454 (2007).
42. Liu, B. & Bazan, G. C. Optimization of the molecular orbital energies of conjugated polymers for optical amplification of fluorescent sensors. *J. Am. Chem. Soc.* **128**, 1188–1196 (2006).
43. Munro, C. H., Smith, W. E., Garner, M., Clarkson, J. & White, P. C. Characterization of the surface of a citrate-reduced colloid optimized for use as a substrate for surface-enhanced resonance Raman scattering. *Langmuir* **11**, 3712–3720 (1995).
44. Zhang, Q. *et al.* Seed-mediated synthesis of Ag nanocubes with controllable edge lengths in the range of 30–200 nm and comparison of their optical properties. *J. Am. Chem. Soc.* **132**, 11372–11378 (2010).
45. Yguerabide, J. & Yguerabide, E. E. Light-scattering submicroscopic particles as highly fluorescent analogs and their use as tracer labels in clinical and biological applications: II. experimental characterization. *Anal. Biochem.* **262**, 157–176 (1998).
46. Hutter, E. & Fendler, J. H. Exploitation of localized surface plasmon resonance. *Adv. Mater.* **16**, 1685–1706 (2004).
47. Wiley, B. J. *et al.* Maneuvering the surface plasmon resonance of silver nanostructures through shape-controlled synthesis. *J. Phys. Chem. B* **110**, 15666–15675 (2006).
48. Fatin-Rouge, N., Milon, A., Buffle, J., Goulet, R. R. & Tessier, A. Diffusion and partitioning of solutes in agarose hydrogels: The relative influence of electrostatic and specific interactions. *J. Phys. Chem. B* **107**, 12126–12137 (2003).
49. Luu, Q. N. *et al.* Preparation and optical properties of silver nanowires and silver-nanowire thin films. *J. Colloid Interface Sci.* **356**, 151–158 (2011).
50. Park, H.-J., Vak, D., Noh, Y.-Y., Lim, B. & Kim, D.-Y. Surface plasmon enhanced photoluminescence of conjugated polymers. *Appl. Phys. Lett.* **90**, 161107 (2007).
51. Geng, J., Liang, J., Wang, Y., Gurdzayan, G. G. & Liu, B. Metal-enhanced fluorescence of conjugated polyelectrolytes with self-assembled silver nanoparticle platforms. *J. Phys. Chem. B* **115**, 3281–3288 (2011).
52. Chen, Y., Munechika, K. & Ginger, D. S. Dependence of fluorescence intensity on the spectral overlap between fluorophores and plasmon resonant single silver nanoparticles. *Nano Lett.* **7**, 690–696 (2007).
53. Ming, T., Chen, H., Jiang, R., Li, Q. & Wang, J. Plasmon-controlled fluorescence: beyond the intensity enhancement. *J. Phys. Chem. Lett.* **3**, 191–202 (2012).
54. Jang, E., Son, K. J., Kim, B. & Koh, W.-G. Phenol biosensor based on hydrogel microarrays entrapping tyrosinase and quantum dots. *Analyst* **135**, 2871–2878 (2010).
55. Steinmetz, R. *et al.* The xenoestrogen bisphenol A induces growth, differentiation, and C-fos gene expression in the female reproductive tract. *Endocrinology* **139**, 2741–2747 (1998).

Acknowledgments

This work was supported by the National Natural Science Foundation of China (51373022), the Program for New Century Excellent Talents in University of Ministry of Education of China (NCET-11-0576), the Program for Changjiang Scholars and Innovative Research Team in University and the State Key Lab for Advanced Metals and Materials (2012-ZD05).

Author contributions

X.W., F.H., X.Z. and F.T.: material preparation and characterization and data analysis. L.L.: project planning, data analysis and writing.

Additional information

Supplementary information accompanies this paper at <http://www.nature.com/scientificreports>

Competing financial interests: The authors declare no competing financial interests.

How to cite this article: Wang, X.Y., He, F., Zhu, X., Tang, F. & Li, L.D. Hybrid silver nanoparticle/conjugated polyelectrolyte nanocomposites exhibiting controllable metal-enhanced fluorescence. *Sci. Rep.* **4**, 4406; DOI:10.1038/srep04406 (2014).



This work is licensed under a Creative Commons Attribution-NonCommercial-ShareAlike 3.0 Unported license. To view a copy of this license, visit <http://creativecommons.org/licenses/by-nc-sa/3.0>